PACE: Geometry-Aware Bridge Transport for Single-Cell Trajectory Inference

Chenglei Yu* [1 2] **Chuanrui Wang*** [2] **Bangyan Liao** [1 2] **Tailin Wu** [2]

Abstract

Single-cell trajectory inference from destructive time-course snapshots is fundamentally ill-posed: neither cross-time cell correspondences nor the continuous paths between snapshots are observed, so the observed snapshot distributions alone do not uniquely determine the underlying dynamics. Existing optimal transport and flow-based methods typically couple cells by Euclidean proximity at observed clock times, which can misalign trajectories when development is asynchronous and cells sampled at the same experimental time occupy different latent pseudotime stages. We propose PACE, a trajectory inference framework that selects geometry-consistent continuous transport dynamics from destructive time-course snapshots through three coupled components. First, PACE constructs a state- and time-dependent anisotropic Riemannian metric that preserves low cost along locally supported tangent directions while penalizing normal velocity components. Second, it alternates between refining cross-time couplings under the induced path-action cost and fitting endpoint-preserving neural bridges between adjacent snapshots. Third, it distills the learned bridge dynamics into a global continuous-time velocity field over cellular states. Across seven controlled and biological datasets covering nine held-out reconstruction experiments, PACE achieves the strongest overall reconstruction performance, reducing MMD, $\mathcal{W}_1$, and $\mathcal{W}_2$ by 23.7% on average relative to the strongest competing baseline. PACE also improves RNA-velocity alignment by 15.4% on an embryoid body differentiation benchmark, without requiring explicit cell pairing, lineage tracing, or RNA velocity supervision during training. Code is available at https://github.com/AI4Science-WestlakeU/PACE.

*Equal contribution [1]Zhejiang University [2]Department of Artificial Intelligence, School of Engineering, Westlake University. Correspondence to: Chenglei Yu <yuchenglei@westlake.edu.cn>, Tailin Wu <wutailin@westlake.edu.cn>.

Accepted at the 2026 Workshop on Generative and Agentic AI for Biology (ICML 2026)

1. Introduction

Understanding how cells move from one state to another is a central problem in single-cell biology (Farrell et al., 2018; Wagner et al., 2018; Schiebinger et al., 2019; Tanay & Regev, 2017; Griffiths et al., 2018). Processes such as development, differentiation, immune activation, tumor evolution, and cellular reprogramming are not simply collections of discrete cell types, but continuous population-level transitions through high-dimensional molecular state space (Trapnell et al., 2014; Haghverdi et al., 2016; Setty et al., 2019; Cacchiarelli et al., 2018). The key questions are therefore dynamical, including which early states commit to particular fates, which intermediate states are transient but decisive, and which regulatory programs drive these transitions. Trajectory inference (Lavenant et al., 2021; Hashimoto et al., 2016) aims to answer these questions by reconstructing continuous cell-state evolution from time-course single-cell observations.

Transport- and flow-based trajectory methods provide a natural framework for modeling such dynamics (Peyré & Cuturi, 2019; Schiebinger et al., 2019; Lavenant et al., 2021). Since time-course single-cell data provide population-level snapshots rather than paired observations of the same cells (Weinreb et al., 2018; Schiebinger et al., 2019), these methods must infer how marginal distributions are coupled across time. Most existing formulations operate in the Euclidean representation space, where couplings are estimated from Euclidean endpoint costs and continuous paths or velocity fields are regularized by Euclidean kinetic energy, action, or smoothness (Neklyudov et al., 2023; Tong et al., 2023; 2020; Huguet et al., 2022). This Euclidean geometry is convenient, but it is not necessarily aligned with biological progress. Two cells can be close in expression space while lying at different developmental stages or fate branches, whereas biologically plausible motion may follow curved and locally anisotropic directions along the cell-state manifold (Moon et al., 2019; Wolf et al., 2019).

This mismatch makes trajectory inference from destructive snapshots fundamentally ambiguous (Weinreb et al., 2018; Tritschler et al., 2019): the cross-time coupling is

not observed and is generally not identifiable from marginal distributions alone. A coupling may satisfy the marginal constraints while connecting cells across incompatible developmental programs, stalled states, or fate branches. For example, in mouse reprogramming (Schiebinger et al., 2019), differences in growth rates between cell types can make marginal matching misleading, coupling apoptotic stromal cells to rapidly expanding iPSCs. Human iPSC reprogramming (Liu et al., 2020) shows the same issue at finer granularity, that cells collected on the same day can contain heterogeneous primed-like, naive-like, and trophectoderm-like intermediates, so clock-time adjacency alone does not determine which cells should be coupled. Auxiliary measurements such as RNA velocity, lineage tracing, or metabolic labeling (La Manno et al., 2018; Bergen et al., 2020; Lange et al., 2022) can help, but require additional experiments and are unavailable in many datasets. Existing Euclidean or support-based regularizers can encourage short, smooth, or data-supported paths (Saelens et al., 2019), but they do not directly encode which local directions of motion are developmentally admissible.

We propose PACE, a geometry-aware trajectory-inference framework for selecting snapshot-consistent continuous transport dynamics from unpaired time-course snapshots. The intuition is that, although true cell identities and intermediate paths are unobserved, local spatiotemporal neighborhoods still provide a weak but useful prior on admissible directions, since motion along locally supported tangent directions is more plausible than motion orthogonal to the observed manifold structure. PACE therefore replaces Euclidean transport costs with a Riemannian path action induced by a state- and time-dependent anisotropic metric, which assigns lower cost to locally supported tangent motion and higher cost to normal motion. Specifically, PACE estimates local tangent *directions* from spatiotemporal neighborhoods of observed cells and uses this metric to define an anisotropic bridge transport problem, where the cost of coupling two cells is the minimum Riemannian action of an endpoint-conditioned path. PACE then alternates between refining OT couplings under this path-action cost and fitting endpoint-preserving neural bridges, allowing local geometry to influence both which cells are coupled and how they move between snapshots. Finally, the learned bridge dynamics are distilled into a continuous-time population velocity field over cellular states.

Our contributions are threefold:

1. We introduce a time- and state-dependent Riemannian metric based on local spatiotemporal tangent-space projections, providing a geometry-aware path-action cost for selecting couplings between adjacent destructive snapshots beyond Euclidean endpoint proximity.
2. We develop an iterative bridge-transport procedure that alternates between Riemannian coupling refinement and endpoint-preserving neural bridge fitting, allowing cross-time correspondences and interpolant paths to be selected jointly under the same geometry-aware action.
3. We distill endpoint-conditioned bridges into a global continuous-time population velocity field and evaluate PACE on seven datasets covering nine held-out reconstruction experiments. PACE achieves the strongest overall reconstruction performance, reducing MMD, $\mathcal{W}_1$, and $\mathcal{W}_2$ by 23.7% on average relative to the strongest competing baseline, improves RNA-velocity alignment on an embryoid body differentiation benchmark, and shows consistent gains across component ablations.

2. Related Work

Optimal transport and flow-based trajectory inference. Optimal transport provides a natural framework for coupling unpaired snapshot distributions in single-cell analysis (Schiebinger et al., 2019; Lavenant et al., 2021). Recent neural extensions such as TrajectoryNet (Tong et al., 2020), Wasserstein Lagrangian Flows (Neklyudov et al., 2023), and Conditional Flow Matching (CFM) (Lipman et al., 2023; Tong et al., 2023) learn continuous dynamics by regressing vector fields along interpolants between coupled endpoints. Schrodinger bridge methods (De Bortoli et al., 2021; Shi et al., 2023; Chen et al., 2023) add stochasticity or entropic regularization to the transport problem, while Curly Flow Matching (Petrović et al., 2026) extends the framework to non-gradient dynamics using approximate velocity information. These methods typically infer couplings from Euclidean proximity or OT distances in the observed space, which can misalign trajectories when cells at the same experimental time occupy different pseudotime stages.

Geometry-aware generative models. The manifold hypothesis has motivated data-dependent Riemannian metrics in ambient spaces (Hauberg et al., 2012; Arvanitidis et al., 2017), flow matching on known manifolds or general geometries (Chen & Lipman, 2024), and manifold-aware OT flows for single-cell trajectories (Huguet et al., 2022). Metric Flow Matching (MFM) (Kapuśniak et al., 2024) is closest to our setting: it uses task-independent *support-aware* metrics such as LAND (Arvanitidis et al., 2017) and RBF to pull geodesics toward the data support. PACE differs in both the source and use of geometry. In asynchronous reprogramming, density support alone does not determine plausible cross-time transitions, since a high-density intermediate may connect to either progressed or refractory fates and Euclidean proximity can couple incompatible programs. PACE instead builds a time- and state-dependent, *direction-aware* metric from local spatiotemporal tangent subspaces

estimated from destructive snapshots, penalizing motion orthogonal to plausible developmental directions. The resulting metric action is used both to learn interpolant paths and to refine cross-time couplings, whereas MFM typically assumes the endpoint pairing is fixed before interpolant learning.

3. Method

3.1. Problem formulation

We observe single-cell point clouds at anchor times $\{t_k\}_{k=0}^{K}$, with $t_0 = 0$,

$$\mathcal{X}^{(k)} = \{x_i^{(k)}\}_{i=1}^{N_k} \sim \hat{\rho}_k \subset \mathbb{R}^d, \qquad k = 0, 1, \ldots, K.$$

Here d denotes the representation dimension. Our goal is to infer trajectories and a velocity field transporting $\hat{\rho}_k$ to $\hat{\rho}_{k+1}$ between adjacent times. Once learned, the velocity field can be integrated from $x_{t_0} \sim \hat{\rho}_0$ to generate trajectories over the time course.

Proposition 3.1 (Ill-posedness from snapshots alone)**.** *Given only the point clouds $\{\mathcal{X}^{(k)}\}_{k=0}^{K}$, the reconstruction of cross-time couplings and intermediate trajectories is non-unique.*

Indeed, for a single interval $[t_k, t_{k+1}]$, many couplings $\pi_k \in \Pi(\hat{\rho}_k, \hat{\rho}_{k+1})$ share the same endpoint marginals. For any such coupling, each coupled endpoint pair can also be connected by infinitely many smooth paths. Thus, the observed snapshots determine neither a unique correspondence nor a unique intermediate trajectory. This observation motivates PACE to frame trajectory inference as a variational problem over couplings and paths, selected by a geometry-aware path action. The proof of Proposition 3.1 is given in Appendix D.

3.2. Geometry-aware bridge transport

To address the ill-posedness in Proposition 3.1, PACE formulates trajectory reconstruction as selecting both a cross-time coupling and a family of continuous paths, chosen by minimizing a geometry-aware action. Given a time- and state-dependent metric tensor $G_k(x, t)$ (constructed in §3.3), the cost of a path γ, or "path action", between endpoints (x, y) is

$$\mathcal{A}_{G_k}[\gamma] = \int_0^1 \dot{\gamma}(\tau)^\top G_k\big(\gamma(\tau),\, t_{k,\tau}\big)\dot{\gamma}(\tau)\, d\tau, \qquad \gamma(0) = x,\ \gamma(1) = y, \tag{1}$$

where $\tau \in [0, 1]$ is local interpolation time and the physical time is $t_{k,\tau} = t_k + \tau(t_{k+1} - t_k)$. The path action first defines the geometry-aware endpoint cost, and the ideal PACE bridge problem then transports mass using this induced cost:

$$\begin{aligned} c_{G_k}(x, y) &= \inf_{\substack{\gamma(0)=x \\ \gamma(1)=y}} \mathcal{A}_{G_k}[\gamma], \\ \pi_k^\star &\in \arg\min_{\pi_k \in \Pi(\hat{\rho}_k, \hat{\rho}_{k+1})} \int c_{G_k}(x, y)\, d\pi_k(x, y). \end{aligned} \tag{2}$$

Here $c_{G_k}(x, y)$ is not a fixed Euclidean endpoint distance; it is the minimum action required to move from x to y under the metric G_k.

This formulation makes explicit how PACE differs from standard OT. If $G_k(x, t) \equiv I$, then Eq. (1) reduces to the Euclidean kinetic energy. For any fixed endpoint pair (x, y), the minimum-action path is the straight constant-speed interpolant, and the induced cost becomes

$$c_{G_k}(x, y) = \|y - x\|^2.$$

In this special case, Eq. (2) reduces to standard quadratic-cost OT between $\hat{\rho}_k$ and $\hat{\rho}_{k+1}$.

PACE departs from this Euclidean case by using a state- and time-dependent anisotropic metric $G_k(x, t)$. The induced cost $c_{G_k}(x, y)$ is no longer determined only by endpoint distance; it depends on the entire path and on how the *path velocity* aligns with local developmental geometry. As a result, the minimum-action cost generally has no closed-form solution and cannot be reduced to a fixed Euclidean endpoint cost. The next section defines the spatiotemporal metric $G_k(x, t)$, and § 3.4 describes how PACE approximates this problem with neural bridges and alternating coupling updates.

Finite-dimensional approximation. Problem (2) is an ideal infinite-dimensional formulation. PACE makes it tractable through two approximations (§3.4): (i) the path family is parameterized by neural bridges γ_θ that satisfy endpoint constraints by construction; (ii) the action integral is approximated on a finite time grid. These yield a finite-dimensional alternating optimization over bridge parameters and correspondence variables.

3.3. Time-dependent spatiotemporal tangent metric

The metric should encode a simple prior: admissible motion should follow directions locally supported by the observed geometry, rather than cut across the cell-state manifold. Although local neighborhoods do not reveal the true direction of time, their dominant variation directions provide an undirected tangent approximation to the set of plausible state changes. PACE therefore treats tangent motion as low cost and penalizes velocity components in the locally estimated normal subspace. Because the local composition and geometry of snapshots can change across experimental time, the admissible subspaces are indexed by both state and time, yielding a time- and state-dependent metric $G_k(x, t)$.

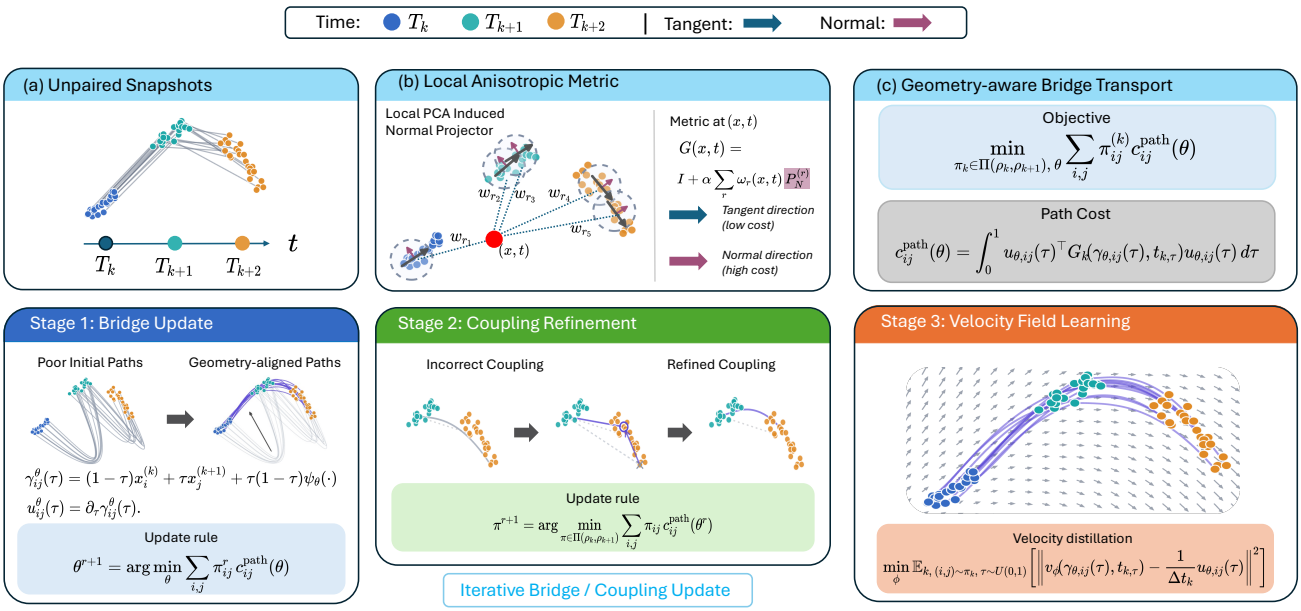

Figure 1. **Overview of PACE.** PACE uses local PCA to construct an anisotropic metric $G_k(x,t) = I + \alpha C_N^{(k)}(x,t)$, trains endpoint-preserving neural bridges under the corresponding path-action cost, iteratively refines cross-time couplings, and distills the learned bridge dynamics into a global velocity field for trajectory inference from unpaired snapshots.

Local normal subspaces. At each anchor point x_r observed at time t_r, PACE estimates an anchor-wise local normal direction by finding its m_{nn} nearest spatial neighbors within the same snapshot (including x_r itself), computing a Gaussian-kernel weighted covariance of the neighbor cloud, and extracting the minimum-variance principal direction n_r. In two dimensions the normal projector is simply $P_N^{(r)} = n_r n_r^\top$; in higher dimensions PACE adaptively selects the tangent-subspace dimension and builds the normal projector as the orthogonal complement (Appendix K).

Spatiotemporal metric construction. For a query point (x,t) in segment k, PACE interpolates these anchor-wise local normal projectors across state and time using space-time Gaussian weights over all anchor points r:

$$\omega_r^{(k)}(x,t) \propto \exp\left(-\frac{\|x - x_r\|^2}{(h_x^{(k)})^2} - \frac{|t - t_r|^2}{(h_t^{(k)})^2} \right), \quad (3)$$

with normalization chosen so that $\sum_r \omega_r^{(k)}(x,t) = 1$, where the bandwidths $h_x^{(k)}$ and $h_t^{(k)}$ are estimated adaptively for each segment (see Appendix L). These weights define an averaged normal projector field and the corresponding metric tensor

$$C_N^{(k)}(x,t) = \sum_r \omega_r^{(k)}(x,t) P_N^{(r)},$$
$$G_k(x,t) = I + \alpha C_N^{(k)}(x,t), \qquad \alpha > 0.$$

The corresponding velocity cost is $v^\top G_k(x,t) v = \|v\|^2 + \alpha\, v^\top C_N^{(k)}(x,t)\, v$. Because $C_N^{(k)}$ is a positive-semidefinite average of local normal projectors, the second term increases the cost most strongly for velocities aligned with nearby estimated normal directions.

Proposition 3.2 (Normal-subspace penalizing property)**.** *For every segment k, query point (x,t), and velocity $v \in \mathbb{R}^d$,*

$$v^\top G_k(x,t) v = \|v\|^2 + \alpha v^\top C_N^{(k)}(x,t) v \geq \|v\|^2. \quad (4)$$

Moreover, if $C_N^{(k)}(x,t) = P_N(x,t)$ is an exact orthogonal projector onto the normal subspace $T_{x,t}^\perp$, and $v = v_T + v_N$ with $v_T \in T_{x,t}$ and $v_N \in T_{x,t}^\perp$, then

$$v^\top G_k(x,t) v = \|v_T\|^2 + (1+\alpha)\|v_N\|^2. \quad (5)$$

Proposition 3.2 shows that the interpolated metric always preserves at least the Euclidean velocity cost, and that tangent motion retains its Euclidean cost while normal motion is penalized by a factor $1+\alpha$ in the ideal projector case. Thus, the metric turns the qualitative principle of geometry-aligned cellular motion into an explicit action functional.

3.4. Finite-dimensional optimization by alternating bridge and OT coupling updates

PACE approximates the anisotropic bridge problem by alternating between an endpoint-conditioned bridge and a cross-time coupling. The coupling determines which endpoint pairs are used to train the bridge, while the bridge

induces a path-action cost for updating the coupling. This creates a bootstrap mechanism in which more plausible couplings provide better endpoint supervision, and better bridges provide a geometry-aware approximation to the endpoint cost used for OT refinement. Since solving a separate minimum-action path problem for every candidate endpoint pair is infeasible under the state- and time-dependent metric $G_k(x,t)$, PACE amortizes path optimization with a shared endpoint-preserving neural bridge $\gamma_\theta(x,y,\tau)$. See Appendix J for a detailed discussion of this alternating procedure.

Endpoint-preserving neural bridge. For an endpoint pair $(x,y) \in \mathbb{R}^d \times \mathbb{R}^d$ and local time $\tau \in [0,1]$, we define

$$\gamma_\theta(x,y,\tau) = (1-\tau)x + \tau y + \tau(1-\tau)\psi_\theta(x,y,\tau), \quad (6)$$

where $\psi_\theta : \mathbb{R}^d \times \mathbb{R}^d \times [0,1] \to \mathbb{R}^d$ is a neural network. The factor $\tau(1-\tau)$ enforces $\gamma_\theta(x,y,0) = x$ and $\gamma_\theta(x,y,1) = y$, so the network only controls the interior deformation of the path (Petrović et al., 2026). The bridge velocity is $u_\theta(x,y,\tau) = \partial_\tau \gamma_\theta(x,y,\tau)$, computed by automatic differentiation. When $\psi_\theta = 0$, the bridge reduces to the straight Euclidean interpolant.

Bridge learning under fixed coupling. Assume that, for each adjacent snapshot pair, a coupling $\pi_k \in \Pi(\hat{\rho}_k, \hat{\rho}_{k+1})$ is given. During the bridge update, endpoint pairs $(x_i^{(k)}, x_j^{(k+1)}) \sim \pi_k$ are sampled from the current coupling. We write $t_{k,\tau} = t_k + \tau(t_{k+1} - t_k)$.

PACE trains the endpoint-preserving bridge by minimizing

$$\mathcal{L}_{\text{bridge}}(\theta) = \lambda_{\text{metric}}\mathcal{L}_{\text{metric}} + \lambda_{\text{reg}}\mathcal{L}_{\text{reg}}. \quad (7)$$

The main term $\mathcal{L}_{\text{metric}}$ is the anisotropic bridge action induced by the spatiotemporal metric G_k. An optional regularization term $\mathcal{L}_{\text{reg}}$ penalizes large normal components and incoherent cross-segment velocities (Appendix G).

The metric-action loss is

$$\mathcal{L}_{\text{metric}} = \mathbb{E}_{k,(x,y)\sim\pi_k}\Bigg[\frac{1}{T}\sum_{\ell=1}^{T} u_\theta^\top G_k(\gamma_\theta(x,y,\tau_\ell), t_{k,\tau_\ell}) \times \nu_\theta(x,y,\tau_\ell)\Bigg], \ \nu_\theta = \nu_\theta(x,y,\tau_\ell). \quad (8)$$

Coupling update under fixed bridge. After the bridge model has been updated under the current coupling, PACE recomputes the coupling using the full path action rather than Euclidean endpoint distance. For a candidate source-target pair $(x_i^{(k)}, x_j^{(k+1)})$, the path-action cost is

$$c_{ij}^{\text{path}}(\theta) = \frac{1}{M}\sum_{m=1}^{M} u_{ij}^\top G_k(\gamma_{ij}, t_{k,\tau_m})\nu_{ij}, \quad (9)$$

where $\nu_{ij} = \nu_\theta(x_i^{(k)}, x_j^{(k+1)}, \tau_m)$ and $\gamma_{ij} = \gamma_\theta(x_i^{(k)}, x_j^{(k+1)}, \tau_m)$. The coupling is then updated by solving

$$\pi_k \leftarrow \arg\min_{\pi_k \in \Pi(\hat{\rho}_k, \hat{\rho}_{k+1})} \sum_{i,j} c_{ij}^{\text{path}}(\theta)\pi_{ij}^{(k)}. \quad (10)$$

Alternating optimization. Given an initial coupling, PACE alternates between two blocks:

1. **Bridge update.** Fix the current couplings $\{\pi_k\}$, sample endpoint pairs $(x_i^{(k)}, x_j^{(k+1)}) \sim \pi_k$, and update θ by taking gradient steps on Eq. (7).
2. **Coupling update.** Fix the current bridge γ_θ, compute the path-action cost matrix in Eq. (9), and update each π_k by solving the OT problem in Eq. (10).

The bridge update learns low-action endpoint-conditioned paths under the current coupling, while the coupling update selects source-target transport using the learned path action. In the idealized finite-dimensional setting where the bridge block is solved exactly for the metric-action objective, these two updates form a monotone block-coordinate descent scheme; Appendix F states this property and relates it to the stochastic neural implementation. In practice, the coupling update is triggered periodically, for example every R_0 epochs.

3.5. Distilling endpoint-conditioned bridges into a global velocity field

The alternating optimization in §3.4 yields endpoint-conditioned bridges $\gamma_\theta(x,y,\tau)$ and τ-velocities $u_\theta(x,y,\tau) = \partial_\tau\gamma_\theta(x,y,\tau)$. These bridges are pair-specific: to query a velocity at an arbitrary state z and time t, one would need to know which endpoint pair (x,y) and interpolation parameter τ generated z. PACE therefore distills the bridge dynamics into a global velocity field $v_\phi(x,t)$ that can be evaluated without reference to a particular endpoint pair.

Distillation objective. For each segment k, we sample $(x,y) \sim \pi_k$ and $\tau \sim \text{Uniform}[0,1]$, set $x_{t_{k,\tau}} = \gamma_\theta(x,y,\tau)$ with $t_{k,\tau} = t_k + \tau\Delta t_k$, and match the global velocity field:

$$\mathcal{L}_{\text{distill}}(\phi) = \mathbb{E}_{k,(x,y)\sim\pi_k}\mathbb{E}_\tau\big[\|v_\phi(x_t, t_{k,\tau}) - \tfrac{u_\theta}{\Delta t_k}\|^2\big], \quad x_t = \gamma_\theta(x,y,\tau), \ u_\theta = u_\theta(x,y,\tau). \quad (11)$$

where $\Delta t_k = t_{k+1} - t_k$ converts τ-velocity to physical-time velocity. Once v_ϕ is learned, continuous trajectories are generated by integrating

$$\frac{dx_t}{dt} = v_\phi(x_t, t), \qquad x_0 \sim \hat{\rho}_0. \quad (12)$$

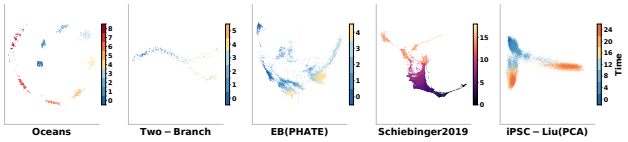

Figure 2. Overview of the 2D benchmark datasets. Points are colored by observed time for Ocean (Petrović et al., 2026), Two-Branch, EB PHATE (Moon et al., 2019), Schiebinger2019 (Schiebinger et al., 2019), and iPSC-Liu (Liu et al., 2020).

Table 1. Per-timepoint results on Ocean (2D) (Petrović et al., 2026), holdout $t \in \{1, 3, 5, 7\}$.

Method	MMD ↓				$\mathcal{W}_1$ ↓				$\mathcal{W}_2$ ↓			
	$t=1$	$t=3$	$t=5$	$t=7$	$t=1$	$t=3$	$t=5$	$t=7$	$t=1$	$t=3$	$t=5$	$t=7$
Action Matching	0.7429	1.0662	0.9465	1.1289	0.3549	0.4823	0.2383	0.5073	0.3662	0.4846	0.2425	0.5143
Aligned CFM	0.7989	0.8754	1.0073	0.8272	0.0976	0.1644	0.3024	0.2245	0.1017	0.1673	0.3046	0.2262
CURLY	1.0545	0.8373	0.5869	0.8663	0.3766	0.1521	0.1077	0.2638	0.3771	0.1537	0.1102	0.2646
DMSB	1.1260	0.6089	0.2542	0.4962	0.3060	0.1097	0.0435	0.1097	0.3065	0.1150	0.0473	0.1142
MFM	0.8482	0.7859	0.6928	0.5823	0.0960	0.1433	0.1359	0.1279	0.0991	0.1452	0.1385	0.1302
OT-CFM	0.9410	0.8169	0.6827	0.6305	0.1227	0.1428	0.1289	0.1321	0.1255	0.1459	0.1308	0.1334
PACE(ours)	**0.4504**	**0.2588**	**0.0735**	**0.2779**	**0.0399**	**0.0398**	**0.0268**	**0.0505**	**0.0440**	**0.0434**	**0.0362**	**0.0534**

4. Experiment

The experiments evaluate PACE through five questions. First, on controlled 2D trajectories, can PACE recover smooth and branching geometry without paired identities or velocity supervision (Figure 2; Tables 1 and A.2)? Second, when reference velocities are available only for evaluation, do the learned dynamics align with held-out velocity fields on Ocean and EB PHATE (Figure 3; Appendix Tables A.3 and A.4)? Third, on biological time courses, does PACE improve held-out reconstruction for single-cell differentiation and reprogramming from destructive snapshots (Table 2)? Fourth, does PACE remain effective as the representation dimension increases (Tables 3)? Finally, which components of PACE account for the observed gains (Figure 5)?

4.1. Experimental setup

Evaluation protocol. All experiments use the same held-out snapshot protocol: methods observe only the training time points and are evaluated on the held-out time points listed in each table caption. We report distributional reconstruction quality using maximum mean discrepancy (MMD), 1-Wasserstein distance ($\mathcal{W}_1$), and 2-Wasserstein distance ($\mathcal{W}_2$); lower is better, bold denotes the best result, and underline denotes the second best.

Datasets. Our benchmark suite includes controlled 2D temporal point clouds and biological single-cell time-course datasets. The controlled datasets are designed to isolate geometric behavior in low-dimensional temporal data, including Ocean (Shen et al., 2025; Petrović et al., 2026) and a branching toy dataset, without relying on cell identities or velocity supervision. The biological datasets test destructive snapshot settings in which individual cell identities are not shared across time, covering embryoid body differentiation (Moon et al., 2019), mouse reprogramming (Schiebinger et al., 2019), induced trophoblast stem-cell reprogramming (Liu et al., 2020), and multimodal CITE-seq/Multiome time courses (Lance et al., 2022). Figure 2 gives a visual overview of the 2D datasets used in the main low-dimensional experiments. Detailed dataset sources and preprocessing choices are provided in Appendix A.

Baselines. We compare against representative transport- and flow-based trajectory models, covering action-based continuous dynamics (Neklyudov et al., 2023), minibatch optimal-transport flow matching (Tong et al., 2023), metric/geodesic flow matching (Kapuśniak et al., 2024), pseudo-velocity-corrected flows (Petrović et al., 2026), adversarial multi-marginal interpolant learning (Kviman et al., 2026), and stochastic Schrödinger bridge dynamics (Chen et al., 2023). Implementation details for baselines and PACE are provided in Appendices B and C. Qualitative prediction-versus-held-out overlays for the same 2D runs are shown in Appendix Figures A.1–A.5.

4.2. Controlled 2D trajectories

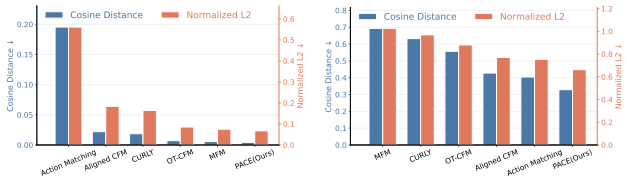

(a) Ocean (b) EB PHATE

Figure 3. Velocity-alignment diagnostics on Ocean (Petrović et al., 2026) and EB PHATE (Moon et al., 2019). Ocean compares learned velocities with held-out simulator velocities, while EB PHATE compares learned 2D velocities with the RNA-velocity reference. Bars report cosine distance and normalized L_2 error; lower is better.

We evaluate PACE on two controlled 2D settings, including Ocean, a rotational non-gradient benchmark from Curly Flow Matching (Petrović et al., 2026), and a Two-Branch toy benchmark. Methods observe only unpaired point positions; simulator velocities and latent identities are not used for training. For Ocean, we also hold out evaluation snapshots and compare the learned velocity field at those times with the simulator velocity field, testing whether the inferred dynamics recover the correct directionality rather than only matching held-out marginals.

Tables 1 and A.2 show that PACE gives the strongest overall held-out reconstruction. It is best on all Ocean metrics and remains strongest on most Two-Branch entries, with CURLY slightly better only for late-branch $\mathcal{W}_2$. The Ocean panel in Figure 3 further checks the learned velocity direction against held-out simulator velocities; the per-timepoint diagnostic values are reported in Appendix Table A.3. Together, these results indicate that the geometry-aware bias

helps recover both smooth rotational motion and simple branching structure from snapshots alone.

4.3. Low-dimensional single-cell trajectories

We next ask whether the same behavior carries over to biological time courses represented in low-dimensional embeddings, where the true cell identities are unobserved and geometric structure must be inferred from destructive snapshots. Table 2 summarizes the time-averaged low-dimensional biological results across EB PHATE, iPSC-Liu, and Schiebinger2019; the corresponding per-timepoint results are reported in Appendix Tables A.5, A.6, and A.7. On EB PHATE, PACE obtains the best MMD, $\mathcal{W}_1$, and $\mathcal{W}_2$, showing that the method improves held-out marginal reconstruction in a manifold-aware PHATE embedding. The EB PHATE panel in Figure 3 adds an independent directionality check by comparing the learned 2D velocity field at the held-out snapshot with RNA velocity, which is used only for evaluation. Appendix Table A.4 shows that PACE also best aligns with this external velocity proxy, suggesting that the gain reflects both endpoint reconstruction and plausible local flow direction. On iPSC-Liu 2D, PACE is best on every reported metric. On Schiebinger2019, PACE is best on seven of nine detailed metric-timepoint entries and remains close on the remaining final-time scores. Overall, the low-dimensional biological results show that PACE transfers the controlled-geometry gains to both differentiation and reprogramming snapshots. Compared with the strongest baseline for each dataset–metric pair, PACE reduces MMD, $\mathcal{W}_1$, and $\mathcal{W}_2$ by 36.2%, 21.5%, and 13.6% on EB PHATE; by 16.1%, 26.4%, and 25.0% on iPSC-Liu; and by 31.2%, 25.5%, and 22.4% on Schiebinger2019.

Table 2. Time-averaged low-dimensional single-cell results. EB (Moon et al., 2019) uses $t = 3$, iPSC-Liu (Liu et al., 2020) uses $t \in \{4, 16\}$, and Schiebinger2019 (Schiebinger et al., 2019) uses $t \in \{6, 11, 16\}$.

Method	EB PHATE			iPSC-Liu			Schiebinger2019		
	MMD ↓	$\mathcal{W}_1$ ↓	$\mathcal{W}_2$ ↓	MMD ↓	$\mathcal{W}_1$ ↓	$\mathcal{W}_2$ ↓	MMD ↓	$\mathcal{W}_1$ ↓	$\mathcal{W}_2$ ↓
Action Matching	0.2436	0.4553	0.5273	0.5230	0.8005	0.9730	0.4057	0.4161	0.4754
Aligned CFM	<u>0.1056</u>	<u>0.2657</u>	<u>0.3243</u>	0.5428	<u>0.6594</u>	<u>0.8320</u>	0.3239	0.3175	0.3931
CURLY	0.1384	0.3223	0.4422	0.5613	0.7186	0.9216	0.7687	1.3684	1.4660
DMSB	0.1325	0.3053	0.4341	0.6456	1.0244	1.1023	<u>0.3030</u>	<u>0.2774</u>	<u>0.3662</u>
MFM	0.1518	0.3704	0.4451	0.5533	0.6657	0.8838	0.6990	1.5897	1.7942
OT-CFM	0.1069	0.2784	0.3622	<u>0.5228</u>	0.7166	0.9261	0.8072	1.9095	2.0235
PACE(ours)	**0.0674**	**0.2087**	**0.2803**	**0.4385**	**0.4853**	**0.6238**	**0.2084**	**0.2067**	**0.2840**

4.4. Higher-dimensional single-cell benchmarks

High-dimensional PCA tests whether PACE still helps when Euclidean distances lose temporal contrast. On iPSC-Liu, PACE is best on all time-averaged 10D/50D metrics in Table 3. On OP-Cite/OP-Multi 100D, it remains on the empirical Pareto front, leading OP-Cite MMD and OP-Multi $\mathcal{W}_1/\mathcal{W}_2$ in Appendix Table A.9. Figure 4 shows the diagnostic behind this regime, with norm CV approaching 0.3 and inter-time separation approaching the within-time radius. The useful signal is therefore not global separation between time means, but local anisotropy within each snapshot; PACE turns that local geometry into coupling costs. This helps distinguish directionally consistent moves from distance-similar but geometrically implausible pairings. Appendix H and Figures A.6–A.7 provide the detailed concentration analysis.

Table 3. iPSC-Liu (Liu et al., 2020) time-averaged results over holdouts $t \in \{4, 8, 12, 16\}$.

Dim	Method	MMD ↓	$\mathcal{W}_1$ ↓	$\mathcal{W}_2$ ↓
10D	Action Matching	0.5555	3.7801	4.3743
	Aligned CFM	<u>0.4644</u>	<u>2.9405</u>	<u>3.3825</u>
	CURLY	0.5369	3.6128	4.2102
	DMSB	0.7713	6.3088	6.4593
	MFM	0.5273	3.4066	3.8382
	OT-CFM	0.5145	3.3850	3.9447
	PACE (ours)	**0.4095**	**2.9226**	**3.1879**
50D	Action Matching	0.3125	7.6126	8.4868
	Aligned CFM	<u>0.2624</u>	<u>7.3133</u>	<u>8.0552</u>
	CURLY	0.3144	8.1144	8.9096
	DMSB	0.5638	10.9368	11.2423
	MFM	0.2853	7.7924	8.5454
	OT-CFM	0.2898	7.8392	8.5954
	PACE (ours)	**0.2550**	**6.7537**	**7.2836**

4.5. Ablation study

We finally isolate the contribution of the main PACE components on the Schiebinger2019 holdouts used in Table A.7. Figure 5 compares the full model with variants that remove coupling rematching, set the metric penalty to the Euclidean case, use all neighbors rather than local neighborhoods, or ablate the spatial and temporal kernel structure used to smooth local geometry. Each simplification degrades at least one metric or time point, and the full PACE variant gives the most stable low errors across MMD, $\mathcal{W}_1$, and $\mathcal{W}_2$. This indicates that the gains do not come from a single implementation detail: the anisotropic metric, local-neighborhood construction, spatial-temporal geometry smoothing, and rematching step all contribute to the final trajectory reconstruction.

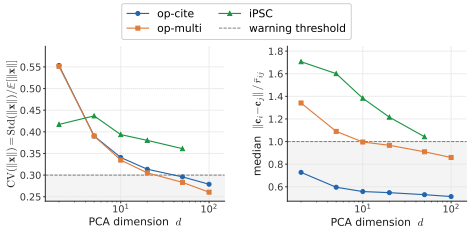

Figure 4. High-dimensional concentration diagnostics. Dashed lines mark norm CV $= 0.3$ and inter-time/within-time ratio $= 1.0$.

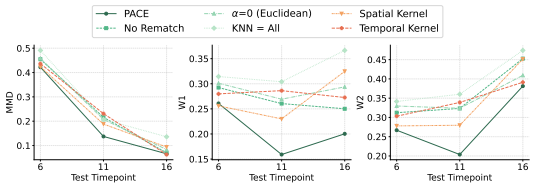

Figure 5. PACE ablations on Schiebinger2019 (Schiebinger et al., 2019) holdouts. Lower is better; variants remove rematching, use Euclidean action ($\alpha = 0$), use all neighbors, or drop spatial/temporal kernels.

5. Conclusion

In this paper, we have introduced PACE, a geometry-aware framework for trajectory inference from destructive single-cell time-course snapshots. PACE replaces fixed Euclidean endpoint costs with an anisotropic path cost induced by a local spatiotemporal metric, then alternates bridge learning with coupling refinement and distills the resulting dynamics into a velocity field. Across controlled and biological benchmarks, the results support local geometry as a useful inductive bias for held-out snapshot reconstruction without paired cells, lineage tracing, or velocity supervision; the velocity diagnostics further show that the learned flows recover plausible directionality when external velocity references are available only for evaluation. Ablations show that this behavior depends on the combination of anisotropic local costs, neighborhood-restricted geometry, smoothing, and coupling rematching rather than a single implementation detail. Future work will focus on more robust metric estimation, uncertainty quantification, and partially supervised or multimodal time-course settings.

References

Arvanitidis, G., Hansen, L. K., and Hauberg, S. Latent space oddity: on the curvature of deep generative models. *arXiv preprint arXiv:1710.11379*, 2017.

Bergen, V., Lange, M., Peidli, S., Wolf, F. A., and Theis, F. J. Generalizing rna velocity to transient cell states through dynamical modeling. *Nature biotechnology*, 38 (12):1408–1414, 2020.

Beyer, K., Goldstein, J., Ramakrishnan, R., and Shaft, U. When is "nearest neighbor" meaningful? In *International conference on database theory*, pp. 217–235. Springer, 1999.

Cacchiarelli, D., Qiu, X., Srivatsan, S., Manfredi, A., Ziller, M., Overbey, E., Grimaldi, A., Grimsby, J., Pokharel, P., Livak, K. J., et al. Aligning single-cell developmental and reprogramming trajectories identifies molecular determinants of myogenic reprogramming outcome. *Cell Systems*, 7(3):258–268, 2018.

Chassignet, E. P., Hurlburt, H. E., Smedstad, O. M., Halliwell, G. R., Hogan, P. J., Wallcraft, A. J., Baraille, R., and Bleck, R. The hycom (hybrid coordinate ocean model) data assimilative system. *Journal of Marine Systems*, 65 (1-4):60–83, 2007.

Chen, R. T. Q. and Lipman, Y. Flow matching on general geometries. In *The Twelfth International Conference on Learning Representations*, 2024. URL https://openreview.net/forum?id=g7ohDlTITL.

Chen, T., Liu, G.-H., Tao, M., and Theodorou, E. Deep momentum multi-marginal schrödinger bridge. *Advances in Neural Information Processing Systems*, 36:57058–57086, 2023.

De Bortoli, V., Thornton, J., Heng, J., and Doucet, A. Diffusion schrödinger bridge with applications to score-based generative modeling. *Advances in neural information processing systems*, 34:17695–17709, 2021.

Farrell, J. A., Wang, Y., Riesenfeld, S. J., Shekhar, K., Regev, A., and Schier, A. F. Single-cell reconstruction of developmental trajectories during zebrafish embryogenesis. *Science*, 360(6392):eaar3131, 2018.

Griffiths, J. A., Scialdone, A., and Marioni, J. C. Using single-cell genomics to understand developmental processes and cell fate decisions. *Molecular systems biology*, 14(4):MSB178046, 2018.

Haghverdi, L., Büttner, M., Wolf, F. A., Buettner, F., and Theis, F. J. Diffusion pseudotime robustly reconstructs lineage branching. *Nature methods*, 13(10):845–848, 2016.

Hashimoto, T., Gifford, D., and Jaakkola, T. Learning population-level diffusions with generative rnns. In *International Conference on Machine Learning*, pp. 2417–2426. PMLR, 2016.

Hauberg, S., Freifeld, O., and Black, M. A geometric take on metric learning. *Advances in Neural Information Processing Systems*, 25, 2012.

Huguet, G., Magruder, D. S., Tong, A., Fasina, O., Kuchroo, M., Wolf, G., and Krishnaswamy, S. Manifold interpolating optimal-transport flows for trajectory inference. *Advances in neural information processing systems*, 35: 29705–29718, 2022.

Kapuśniak, K., Potaptchik, P., Reu, T., Zhang, L., Tong, A., Bronstein, M., Bose, A. J., and Di Giovanni, F. Metric flow matching for smooth interpolations on the data manifold. *Advances in Neural Information Processing Systems*, 37:135011–135042, 2024.

Kviman, O., Tamogashev, K., Branchini, N., Elvira, V., Lagergren, J., and Malkin, N. Multi-marginal flow matching with adversarially learnt interpolants. In *The Fourteenth International Conference on Learning Representations*, 2026. URL https://openreview.net/forum?id=AJls43yje7.

La Manno, G., Soldatov, R., Zeisel, A., Braun, E., Hochgerner, H., Petukhov, V., Lidschreiber, K., Kastriti, M. E., Lönnerberg, P., Furlan, A., et al. Rna velocity of single cells. *Nature*, 560(7719):494–498, 2018.

Lance, C., Luecken, M. D., Burkhardt, D. B., Cannoodt, R., Rautenstrauch, P., Laddach, A., Ubingazhibov, A., Cao, Z.-J., Deng, K., Khan, S., et al. Multimodal single cell data integration challenge: results and lessons learned. *BioRxiv*, pp. 2022–04, 2022.

Lange, M., Bergen, V., Klein, M., Setty, M., Reuter, B., Bakhti, M., Lickert, H., Ansari, M., Schniering, J., Schiller, H. B., et al. Cellrank for directed single-cell fate mapping. *Nature methods*, 19(2):159–170, 2022.

Lavenant, H., Zhang, S., Kim, Y.-H., and Schiebinger, G. Towards a mathematical theory of trajectory inference. *arXiv preprint arXiv:2102.09204*, 2021.

Ledoux, M. *The concentration of measure phenomenon*. Number 89. American Mathematical Soc., 2001.

Lipman, Y., Chen, R. T. Q., Ben-Hamu, H., Nickel, M., and Le, M. Flow matching for generative modeling. In *The Eleventh International Conference on Learning Representations*, 2023. URL https://openreview.net/forum?id=PqvMRDCJT9t.

Liu, X., Ouyang, J. F., Rossello, F. J., Tan, J. P., Davidson, K. C., Valdes, D. S., Schroeder, J., Sun, Y. B., Chen, J., Knaupp, A. S., et al. Reprogramming roadmap reveals route to human induced trophoblast stem cells. *Nature*, 586(7827):101–107, 2020.

Moon, K. R., Van Dijk, D., Wang, Z., Gigante, S., Burkhardt, D. B., Chen, W. S., Yim, K., Elzen, A. v. d., Hirn, M. J., Coifman, R. R., et al. Visualizing structure and transitions in high-dimensional biological data. *Nature biotechnology*, 37(12):1482–1492, 2019.

Neklyudov, K., Brekelmans, R., Severo, D., and Makhzani, A. Action matching: Learning stochastic dynamics from samples. In *International conference on machine learning*, pp. 25858–25889. PMLR, 2023.

Petrović, K., Atanackovic, L., Moro, V., Kapuśniak, K., Ceylan, I. I., Bronstein, M. M., Bose, J., and Tong, A. Curly flow matching for learning non-gradient field dynamics. In *The Thirty-ninth Annual Conference on Neural Information Processing Systems*, 2026. URL https://openreview.net/forum?id=7cqKVDgFZQ.

Peyré, G. and Cuturi, M. *Computational optimal transport: With applications to data science*. Now Foundations and Trends, 2019.

Saelens, W., Cannoodt, R., Todorov, H., and Saeys, Y. A comparison of single-cell trajectory inference methods. *Nature biotechnology*, 37(5):547–554, 2019.

Schiebinger, G., Shu, J., Tabaka, M., Cleary, B., Subramanian, V., Solomon, A., Gould, J., Liu, S., Lin, S., Berube, P., et al. Optimal-transport analysis of single-cell gene expression identifies developmental trajectories in reprogramming. *Cell*, 176(4):928–943, 2019.

Setty, M., Kiseliovas, V., Levine, J., Gayoso, A., Mazutis, L., and Pe'Er, D. Characterization of cell fate probabilities in single-cell data with palantir. *Nature biotechnology*, 37(4):451–460, 2019.

Shen, Y., Berlinghieri, R., and Broderick, T. Multi-marginal schrödinger bridges with iterative reference refinement. In *The 28th International Conference on Artificial Intelligence and Statistics*, 2025. URL https://openreview.net/forum?id=VcwZ3gtYFY.

Shi, Y., De Bortoli, V., Campbell, A., and Doucet, A. Diffusion schrödinger bridge matching. *Advances in neural information processing systems*, 36:62183–62223, 2023.

Tanay, A. and Regev, A. Scaling single-cell genomics from phenomenology to mechanism. *Nature*, 541(7637):331–338, 2017.

Tong, A., Huang, J., Wolf, G., Van Dijk, D., and Krishnaswamy, S. Trajectorynet: A dynamic optimal transport network for modeling cellular dynamics. In *International conference on machine learning*, pp. 9526–9536. PMLR, 2020.

Tong, A., Malkin, N., Huguet, G., Zhang, Y., Rector-Brooks, J., Fatras, K., Wolf, G., and Bengio, Y. Conditional flow matching: Simulation-free dynamic optimal transport. *arXiv preprint arXiv:2302.00482*, 2(3), 2023.

Trapnell, C., Cacchiarelli, D., Grimsby, J., Pokharel, P., Li, S., Morse, M., Lennon, N. J., Livak, K. J., Mikkelsen,

T. S., and Rinn, J. L. The dynamics and regulators of cell fate decisions are revealed by pseudotemporal ordering of single cells. *Nature biotechnology*, 32(4):381–386, 2014.

Tritschler, S., Büttner, M., Fischer, D. S., Lange, M., Bergen, V., Lickert, H., and Theis, F. J. Concepts and limitations for learning developmental trajectories from single cell genomics. *Development*, 146(12):dev170506, 2019.

Vershynin, R. *High-dimensional probability: An introduction with applications in data science*, volume 47. Cambridge university press, 2018.

Wagner, D. E., Weinreb, C., Collins, Z. M., Briggs, J. A., Megason, S. G., and Klein, A. M. Single-cell mapping of gene expression landscapes and lineage in the zebrafish embryo. *Science*, 360(6392):981–987, 2018.

Weinreb, C., Wolock, S., Tusi, B. K., Socolovsky, M., and Klein, A. M. Fundamental limits on dynamic inference from single-cell snapshots. *Proceedings of the National Academy of Sciences*, 115(10):E2467–E2476, 2018.

Wolf, F. A., Hamey, F. K., Plass, M., Solana, J., Dahlin, J. S., Göttgens, B., Rajewsky, N., Simon, L., and Theis, F. J. Paga: graph abstraction reconciles clustering with trajectory inference through a topology preserving map of single cells. *Genome biology*, 20(1):59, 2019.

Technical appendices and supplementary material

A. Benchmark and Metric Details 11

B. Baseline Details 16

C. PACE Implementation Details 16

D. Proof of Proposition 3.1 (Ill-posedness) 17

E. Local Metric and Correspondence 17

F. Monotonicity of Ideal Alternating Updates 17

G. Stage 1 Regularizers 18

H. High-Dimensional Concentration Effects 18

I. iPSC-Liu Results 19

J. Intuition behind alternating bridge and coupling optimization 20

K. Adaptive tangent and normal projectors 20

L. Adaptive bandwidth estimation 20

M. Limitations and Future Work 21

A. Benchmark and Metric Details

All datasets are cast as unpaired time-course point clouds. A point is a cell or synthetic particle state, and a time point is an empirical marginal distribution. Methods receive only the training snapshots; held-out snapshots are used only for evaluation. No method receives cell identities, cross-time correspondences, RNA velocity, or any ground-truth trajectory pairing.

Shared split and rollout protocol. For a held-out label t_h, the evaluator finds the nearest observed training labels $t_a < t_h < t_b$. The learned velocity field is rolled out from the empirical source cloud at t_a toward t_b on the same normalized training-time scale used during training. We use 101 Euler ODE steps and extract the intermediate frame at ratio $(t_h - t_a)/(t_b - t_a)$. The predicted cloud is then compared with the empirical held-out cloud at t_h. Thus, the reported numbers measure recovery of the missing marginal distribution, not recovery of unobserved cell identities.

Ocean benchmark. The Ocean benchmark follows the Gulf of Mexico vortex experiment of Shen et al. (Shen et al., 2025). The data are generated by first extracting a velocity field around a vortex feature from high-resolution HYbrid Coordinate Ocean Model (HYCOM) reanalysis data (Chassignet et al., 2007), then simulating particles representing buoys or ocean debris through that field. The original benchmark contains approximately 1000 observations across five training times and four validation times; the released array used here has nine snapshots with 111 particles per snapshot. Unlike the reference-family model in Shen et al., PACE and all baselines in our comparison receive only the particle positions at training snapshots, with no velocity supervision. The HYCOM-derived velocity field is held out from training and used only for the velocity-alignment diagnostic in Table A.3.

Velocity-alignment diagnostics. Figure 3 summarizes the velocity-alignment checks used in the main experiments. The tables below report the numerical values behind the two panels: Ocean compares learned velocities with held-out simulator velocities, while EB PHATE compares learned 2D velocities with the RNA-velocity reference. These reference velocities are used only for diagnostics, not for training.

Low-dimensional single-cell reconstruction results. Table 2 reports the time-averaged summary used in the main text. The tables below give the corresponding per-timepoint results for each low-dimensional biological benchmark: EB PHATE has one held-out PHATE snapshot, iPSC-Liu has two held-out 2D PCA snapshots, and Schiebinger2019 has three held-out reprogramming days. These detailed tables show whether the averaged gains are consistent across individual held-out times.

Subsampling and dimensionality. For biological datasets, `samples_per_timepoint` is either an experiment-specific cap or `null`. When it is a cap, each selected time point is sampled without replacement using the experiment seed before whitening. When it is `null`, all available cells from the selected time points are used. For EB, the raw timepoint counts are $2381, 4163, 3278, 3665, 3332$ across labels $0, \ldots, 4$. For iPSC-Liu and OP-Cite/OP-Multi, the dimensionality is chosen by taking the first d PCA coordinates from `X_pca`. The 10D and 50D iPSC-Liu tables aggregate separate single-holdout runs; in each run the held-out label is removed from the training label set.

Metrics. For every held-out time point, we compare the predicted point cloud with the observed point cloud using three distributional metrics. MMD is computed with a Gaussian kernel and a median-heuristic bandwidth, and the reported value is the square root of the nonnegative MMD estimate. $\mathcal{W}_1$ uses uniform empirical weights and the Euclidean ground cost between predicted and observed samples. $\mathcal{W}_2$ uses uniform empirical weights and squared Euclidean ground cost, then reports the square root of the optimal transport value. These metrics are distributional: they evaluate reconstruction of the held-out marginal distribution,

Table A.1. Dataset sources, representations, and held-out splits used in Section 4. Controlled 2D coordinates are used directly. Biological embeddings are standardized by fitting a `StandardScaler` on training snapshots only, then applying it to train and held-out snapshots.

Benchmark	Source and role	Representation and preprocessing	Train/test labels
Ocean (Gulf of Mexico vortex)	HYCOM-derived particle benchmark from Shen et al. (Shen et al., 2025), also used in CURLY (Petrović et al., 2026). Training uses only particle positions; velocities are not used for supervision.	`data/oceans/oceans.npz`; `positions` has shape $(9, 111, 2)$. No whitening; full frames are used.	Train $\{0, 2, 4, 6, 8\}$; test $\{1, 3, 5, 7\}$.
Two-Branch	In-house synthetic bifurcation generated by `src/data_preprocess/generate_two_branch_data.py`. It tests recovery of a trunk that splits into two branches.	Six 2D frames, 64 points per frame, with latent pseudotime and branch labels stored for diagnostics but not given to methods. No whitening; full frames are used.	Train $\{0, 2, 3, 5\}$; test $\{1, 4\}$.
EB PHATE	Embryoid body differentiation data from PHATE (Moon et al., 2019). It represents a low-dimensional differentiation trajectory.	`data/eb_velocity_v5.npz`; 16,819 cells with `phate` $(N, 2)$ and `pcs` $(N, 100)$. The 2D experiment uses PHATE and fits whitening on training cells only.	Train $\{0, 1, 2, 4\}$; test $\{3\}$.
Schiebinger2019	Mouse reprogramming time course from Schiebinger et al. (Schiebinger et al., 2019), converted from the scNODE data package using serum-filtered FLE coordinates.	Local H5AD file; `X` stores 2D FLE coordinates and `obs["day"]` stores integer day labels. Whitening is fit on training cells only.	Train all integer days $0, \ldots, 18$ except $\{6, 11, 16\}$; test $\{6, 11, 16\}$.
iPSC-Liu	Human reprogramming time course from Liu et al. (Liu et al., 2020). It is used to evaluate missing-timepoint reconstruction in PCA representations.	`data/iPSC_liu_pca.h5ad`; `obsm["X_pca"]` provides PCA scores and `obs["timepoint"]` stores labels such as `D0`, parsed as integers. Whitening is fit on training cells only.	2D: train $\{0, 8, 12, 20, 24\}$, test $\{4, 16\}$. 10D/50D: separate single-holdout runs for $t \in \{4, 8, 12, 16\}$.
OP-Cite/OP-Multi	NeurIPS Open Problems multimodal single-cell integration challenge data (Lance et al., 2022). OP-Cite uses CITE-seq features; OP-Multi uses Multiome features.	`op_cite_inputs_0.h5ad` and `op_train_multi_targets_0.h5ad`; both use `obsm["X_pca"]`. Table A.9 uses all 100 PCs, with whitening fit on training cells only.	Train $\{2, 4, 7\}$; test $\{3\}$.

Table A.2. Branching toy (2D) per-timepoint results, holdout $t \in \{1, 4\}$.

Method	MMD ↓		$\mathcal{W}_1$ ↓		$\mathcal{W}_2$ ↓	
	$t=1$	$t=4$	$t=1$	$t=4$	$t=1$	$t=4$
Action Matching	0.6129	0.2905	0.3343	0.2732	0.3419	0.3048
Aligned CFM	0.6524	0.3439	0.3874	0.309	0.3944	0.3371
CURLY	0.2664	0.0767	0.1703	0.1797	0.2123	**0.2087**
DMSB	1.0232	1.1585	4.5832	2.8358	4.5845	2.8406
MFM	0.3817	0.1145	0.1686	0.1865	0.1832	0.2116
OT-CFM	0.5279	0.1244	0.2433	0.1841	0.2509	0.2119
PACE(ours)	**0.1968**	**0.0146**	**0.1386**	**0.1752**	**0.1686**	0.2236

Table A.3. Ocean (Petrović et al., 2026) velocity-alignment diagnostics on held-out time points. The simulator velocity is used only for evaluation. Cosine distance is $1 - \cos(\hat{v}, v)$, and normalized L_2 compares unit-normalized velocity directions; lower is better.

Method	Cosine distance ↓					Normalized L_2 ↓				
	$t=1$	$t=3$	$t=5$	$t=7$	Avg.	$t=1$	$t=3$	$t=5$	$t=7$	Avg.
Action Matching	0.3535	0.0408	0.1974	0.1900	0.1954	0.8174	0.2317	0.5965	0.5993	0.5612
Aligned CFM	0.0440	0.0269	0.0101	0.0073	0.0221	0.2808	0.2118	0.1311	0.1122	0.1840
CURLY	0.0227	0.0068	0.0220	0.0231	0.0186	0.1997	0.0906	0.1709	0.1955	0.1642
MFM	**0.0029**	0.0063	0.0089	0.0043	0.0056	**0.0417**	0.0913	0.0965	0.0698	0.0748
OT-CFM	0.0040	0.0101	0.0088	0.0058	0.0072	0.0738	0.1147	0.0731	0.0801	0.0854
PACE(ours)	0.0041	**0.0030**	**0.0069**	**0.0031**	**0.0043**	0.0756	**0.0631**	**0.0671**	**0.0633**	**0.0673**

Table A.4. EB PHATE (Moon et al., 2019) velocity-alignment diagnostics at the held-out snapshot $t = 3$. The RNA-velocity reference is used only for evaluation. Cosine distance is $1 - \cos(\hat{v}, v)$, and normalized L_2 compares unit-normalized velocity directions; lower is better.

Method	Cosine distance ↓	Normalized L_2 ↓
Action Matching	0.4041	0.7542
Aligned CFM	0.4273	0.7707
CURLY	0.6325	0.9693
MFM	0.6930	1.0261
OT-CFM	0.5571	0.8807
PACE(ours)	**0.3287**	**0.6630**

Table A.5. Per-timepoint results on EB PHATE (Moon et al., 2019) (2D), holdout $t = 3$.

Method	MMD ↓	$\mathcal{W}_1$ ↓	$\mathcal{W}_2$ ↓
	$t=3$	$t=3$	$t=3$
Action Matching	0.2436	0.4553	0.5273
Aligned CFM	0.1056	0.2657	0.3243
CURLY	0.1384	0.3223	0.4422
DMSB	0.1325	0.3053	0.4341
MFM	0.1518	0.3704	0.4451
OT-CFM	0.1069	0.2784	0.3622
PACE(ours)	**0.0674**	**0.2087**	**0.2803**

Table A.6. Per-timepoint results on iPSC-Liu (Liu et al., 2020) (2D), holdout $t \in \{4, 16\}$.

Method	MMD ↓		$\mathcal{W}_1$ ↓		$\mathcal{W}_2$ ↓	
	$t=4$	$t=16$	$t=4$	$t=16$	$t=4$	$t=16$
Action Matching	0.7369	0.3090	0.9719	0.6290	1.0726	0.8733
Aligned CFM	0.8265	0.2590	0.7781	0.5407	0.7858	0.8781
CURLY	0.8156	0.3069	0.9030	0.5341	0.9292	0.9140
DMSB	0.8663	0.4248	0.7176	1.3311	0.7986	1.4060
MFM	0.8334	0.2731	0.7646	0.5667	0.7860	0.9815
OT-CFM	0.7787	0.2668	0.8695	0.5636	0.8983	0.9539
PACE(ours)	**0.6808**	**0.1962**	**0.5579**	**0.4126**	**0.5646**	**0.6830**

not cell-wise recovery of unobserved identities.

Table A.7. Per-timepoint results on Schiebinger2019 (Schiebinger et al., 2019), holdout $t \in \{6, 11, 16\}$.

Method	MMD ↓			$\mathcal{W}_1$ ↓			$\mathcal{W}_2$ ↓		
	$t=6$	$t=11$	$t=16$	$t=6$	$t=11$	$t=16$	$t=6$	$t=11$	$t=16$
Action Matching	0.5056	0.4940	0.2174	0.3203	0.4982	0.4298	0.3283	0.5337	0.5642
Aligned CFM	0.5712	0.3405	**0.0601**	0.4126	0.3173	0.2228	0.4291	0.3737	**0.3764**
CURLY	0.9308	1.0201	0.3553	1.4737	1.9135	0.7182	1.5113	1.9386	0.9481
DMSB	0.5081	0.3196	0.0813	0.3118	0.3108	0.2096	0.3174	0.3760	0.4051
MFM	0.8676	0.8858	0.3437	2.6083	1.4602	0.7005	3.0265	1.4793	0.8768
OT-CFM	1.1550	1.0005	0.2661	3.1652	1.8933	0.6701	3.2608	1.9239	0.8856
PACE(ours)	**0.4219**	**0.1373**	0.0660	**0.2609**	**0.1590**	**0.2003**	**0.2669**	**0.2037**	0.3813

Qualitative Stage-2 trajectory visualizations. Figures A.1–A.5 complement the quantitative tables with selected 2D Stage-2 rollouts. For each dataset, the trajectory panel shows the learned rollout geometry for each baseline, while the prediction panel overlays the predicted held-out marginal with the empirical held-out snapshot. These plots are qualitative diagnostics only; all models are trained from unpaired snapshots without cell identities or ground-truth trajectories.

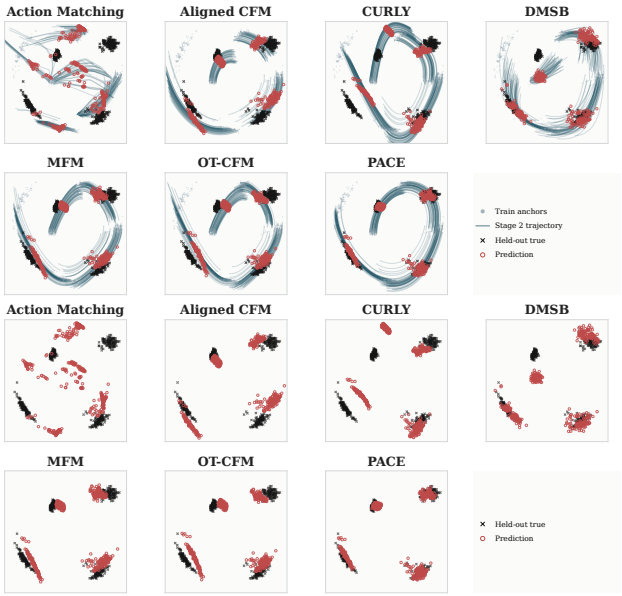

Figure A.1. Qualitative Stage-2 results on Ocean (Shen et al., 2025; Petrović et al., 2026). The top panel shows baseline rollouts; the bottom panel compares predicted and held-out point clouds.

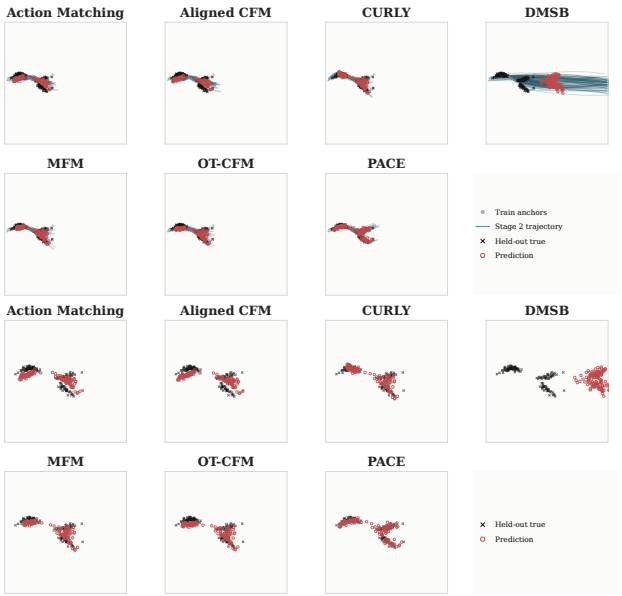

Figure A.2. Qualitative Stage-2 results on the Two-Branch toy benchmark. The top panel shows baseline rollouts; the bottom panel compares predicted and held-out point clouds.

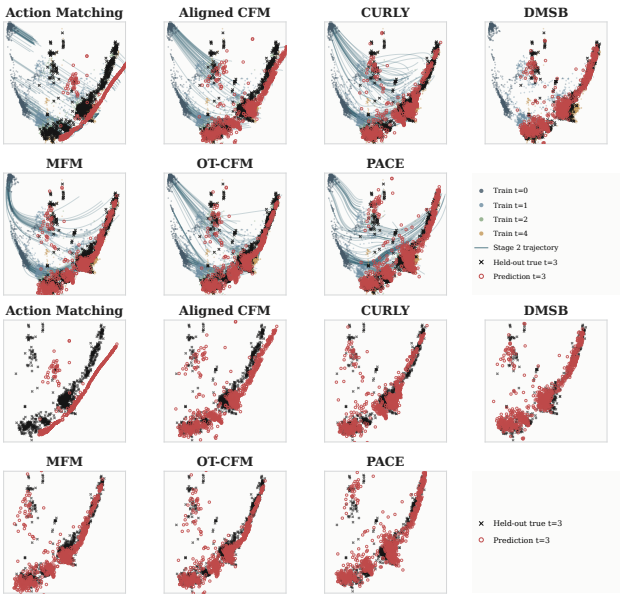

Figure A.3. Qualitative Stage-2 results on EB PHATE (Moon et al., 2019). The top panel shows baseline rollouts; the bottom panel compares predicted and held-out point clouds.

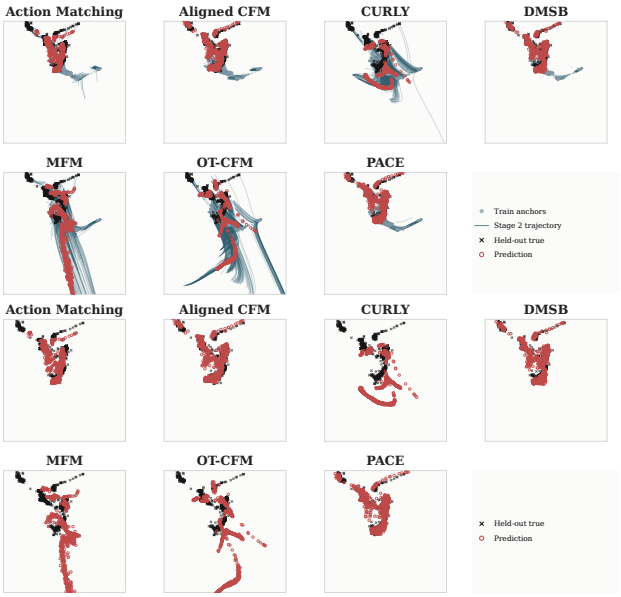

Figure A.4. Qualitative Stage-2 results on Schiebinger2019 (Schiebinger et al., 2019). The top panel shows baseline rollouts; the bottom panel compares predicted and held-out point clouds.

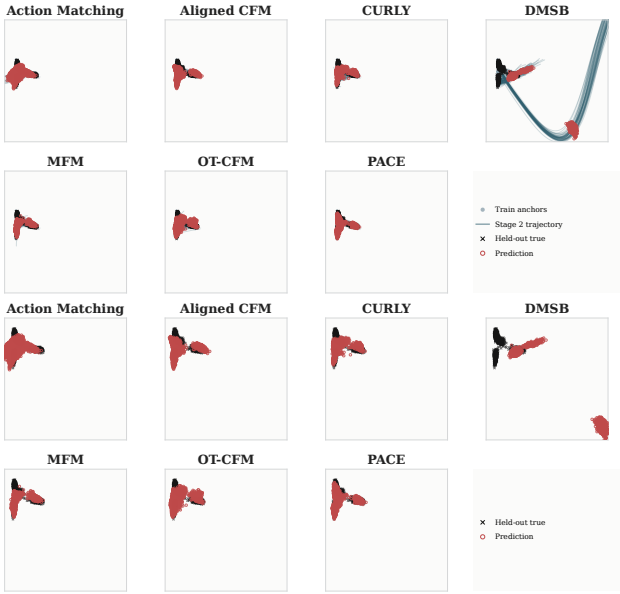

Figure A.5. Qualitative Stage-2 results on iPSC-Liu (Liu et al., 2020). The top panel shows baseline rollouts; the bottom panel compares predicted and held-out point clouds.

B. Baseline Details

The result tables include only methods that were run for the corresponding experiment. All deterministic flow baselines use the same dataloaders, train/test labels, whitening rules, and held-out ODE rollout evaluator described in Appendix A. Unless an experiment-specific config overrides it, flow networks are MLP velocity fields trained with Adam/AdamW-style optimizers. The formulas below describe the implemented objectives under a segment $[t_k, t_{k+1}]$, with $\Delta t = t_{k+1} - t_k$ and normalized segment time $s = (t - t_k)/\Delta t \in [0, 1]$.

Action Matching. Action Matching (Neklyudov et al., 2023) learns a scalar action network $S_\theta(t, x)$. For endpoint samples (x_0, x_1) and an interpolated point $x_t = (1-s)x_0 + sx_1$, the implemented segment loss has the form

$$\begin{aligned}\mathcal{L}_{\mathrm{AM}} = \mathbb{E}\big[&w(t_k)S_\theta(t_k, x_0) \\ &- w(t_{k+1})S_\theta(t_{k+1}, x_1) + \Delta t\, w(t)\partial_t S_\theta(t, x_t) \\ &+ \tfrac{\Delta t}{2} w(t)\|\nabla_x S_\theta(t, x_t)\|^2 + \Delta t\, S_\theta(t, x_t)\partial_t w(t)\big].\end{aligned} \tag{13}$$

At test time, the velocity is $v_\theta(t, x) = \nabla_x S_\theta(t, x)$ and predictions are generated by solving $\dot{x}_t = v_\theta(t, x_t)$.

OT-CFM. OT-CFM (Tong et al., 2023) pairs mini-batches by an optimal-transport plan

$$\pi_k^* \in \arg\min_{\pi \in \Pi(\hat{\rho}_k, \hat{\rho}_{k+1})} \mathbb{E}_{(x_0, x_1)\sim\pi}\|x_0 - x_1\|^2. \tag{14}$$

For paired endpoints, it uses the straight conditional path

$$x_t = (1-s)x_0 + sx_1, \qquad u_t = \frac{x_1 - x_0}{\Delta t}, \tag{15}$$

and trains a velocity network with the flow-matching objective $\mathbb{E}\|v_\theta(t, x_t) - u_t\|^2$. The implementation uses the exact minibatch OT matcher from `torchcfm` and sets the conditional path noise to zero.

MFM. Metric Flow Matching (Kapuśniak et al., 2024) uses a two-stage pipeline. It first trains a geodesic correction network ψ_η under a data-induced metric, then trains a velocity field using the corrected interpolant

$$\mu_t = (1-s)x_0 + sx_1 + \gamma(t)\psi_\eta(x_0, x_1, t), \tag{16}$$

where $\gamma(t)$ vanishes at the segment endpoints. The flow-matching target is the time derivative

$$u_t = \frac{x_1 - x_0}{\Delta t} + \dot{\gamma}(t)\psi_\eta(x_0, x_1, t) + \gamma(t)\partial_t\psi_\eta(x_0, x_1, t), \tag{17}$$

with the last term present when the correction network depends explicitly on time. Our runs use the LAND-style data-manifold metric configuration.

CURLY. CURLY (Petrović et al., 2026) uses a related corrected interpolant, but with the normalized-time modulation $s(1-s)$:

$$\mu_t = (1-s)x_0 + sx_1 + s(1-s)\psi_\eta(x_0, x_1, s). \tag{18}$$

The target velocity used for the second-stage flow model is

$$u_t = \frac{1}{\Delta t}\left[(x_1 - x_0) + (1-2s)\psi_\eta + s(1-s)\partial_s\psi_\eta\right]. \tag{19}$$

The first stage fits ψ_η using pseudo-velocity supervision estimated from the observed temporal point clouds.

Aligned CFM. Aligned CFM follows the adversarially learned interpolant approach of ALI-CFM (Kviman et al., 2026). It trains a global interpolant $I_\eta(x_0, x_1, t)$ from the first to the last training snapshot. Intermediate marginals of I_η are aligned with observed training snapshots by an adversarial objective of the schematic form

$$\begin{aligned}\min_\eta \max_D \sum_\ell \Big[&\mathbb{E}_{x\sim\hat{\rho}_\ell} \log D_\ell(x) \\ &+ \mathbb{E}_{x_0, x_1} \log(1 - D_\ell(I_\eta(x_0, x_1, t_\ell)))\Big].\end{aligned} \tag{20}$$

After this stage, the interpolant is frozen and a velocity model is trained with

$$\mathcal{L}_{\mathrm{ALI-CFM}} = \mathbb{E}\|v_\theta(t, I_\eta(x_0, x_1, t)) - \partial_t I_\eta(x_0, x_1, t)\|^2. \tag{21}$$

DMSB. DMSB (Chen et al., 2023) is a stochastic bridge baseline in joint position-velocity state space $z_t = (x_t, v_t)$. The implementation uses a momentum SDE discretization with learned control $a_\theta(z_t, t)$:

$$z_{n+1} = z_n + \begin{bmatrix} v_n \\ 0 \end{bmatrix}\Delta t + \sigma \begin{bmatrix} 0 \\ a_\theta \Delta t + \epsilon_n \end{bmatrix}, \tag{22}$$

with $a_\theta = a_\theta(z_n, t_n)$ and $\epsilon_n \sim \mathcal{N}(0, \Delta t I)$. Forward and backward policies are trained on the temporal grid, and the learned dynamics are rolled out to predict the held-out marginal distributions. DMSB appears only in the tables where this baseline was run.

C. PACE Implementation Details

PACE is implemented as a two-stage procedure. Stage 1 learns endpoint-preserving bridges and refines the cross-time matching; Stage 2 freezes the learned bridge correction and distills it into a global ODE velocity field for rollout. All reported experiments were run on a single NVIDIA A100 80GB GPU.

Stage 1 anchor construction. For each experiment, the selected training frames are first grouped by time label. PACE stacks the training frames into an anchor tensor of shape $K \times N \times d$, where K is the number of training labels and N is the minimum selected cell count across training time points. If time points have unequal counts, each frame is trimmed to this common N for the Stage 1 matching problem. This produces one adjacent matching problem per training interval.

Initial and refined matchings. The initial matching between adjacent anchors uses a cost combining normalized squared Euclidean distance with the local normal-direction penalty. After a fixed number of bridge-training epochs, PACE recomputes the matching by evaluating the learned path-action cost and solving the induced OT problem. We use the Python Optimal Transport (POT) package for OT computations. Rematching is repeated at a fixed experiment-specific interval (we usually choose 10 or 20), so bridge learning and correspondence estimation alternate throughout training.

Bridge and flow distillation. For endpoints (x_0, x_1) and local time s, the bridge has the endpoint-preserving form

$$\gamma_\theta(x_0, x_1, s) = (1-s)x_0 + sx_1 + s(1-s)\psi_\theta(x_0, x_1, s). \tag{23}$$

The bridge velocity $\partial_s \gamma_\theta$ is obtained by automatic differentiation in 2D and by a Jacobian-vector product implementation in higher dimensions. After Stage 1, ψ_θ is frozen. Stage 2 samples paired endpoints from the Stage 1 matchings and trains a global velocity network $v_\phi(t, x)$ by regressing to the bridge velocity along generated points. Held-out predictions in the tables are produced by rolling out this Stage 2 velocity field.

D. Proof of Proposition 3.1 (Ill-posedness)

Proof of Proposition 3.1. For one interval $[t_k, t_{k+1}]$, many couplings $\pi_k \in \Pi(\hat{\rho}_k, \hat{\rho}_{k+1})$ can share the same endpoint marginals $\hat{\rho}_k$ and $\hat{\rho}_{k+1}$. For any such coupling, each coupled endpoint pair (x, y) can be connected by infinitely many C^1 paths $\gamma : [0,1] \to \mathbb{R}^d$ with $\gamma(0) = x$ and $\gamma(1) = y$. Therefore, the observed snapshots determine neither a unique coupling nor a unique intermediate trajectory. □

E. Local Metric and Correspondence

The metric used by PACE changes the matching criterion from endpoint proximity to path plausibility. In the locally constant idealization, suppose

$$G = I + \alpha P_N, \qquad \alpha > 0,$$

where P_N is the orthogonal projector onto the local normal subspace. For a straight candidate displacement $d = y - x$, the metric action is

$$d^\top G d = \|d\|^2 + \alpha \|P_N d\|^2. \tag{24}$$

Thus, two candidate matches with the same Euclidean distance are not equivalent: the one whose displacement is more tangent-aligned has lower action. The implemented initial matching uses this principle through a normal-projection penalty, while the refined matching applies the same idea to the learned curved bridge by averaging

$$\dot{\gamma}_\theta(s)^\top G(\gamma_\theta(s), t(s)) \dot{\gamma}_\theta(s) \tag{25}$$

over a finite probe grid. This is the practical reason PACE can prefer a slightly longer but tangent-compatible path over a shorter chord that cuts across the inferred developmental geometry.

F. Monotonicity of Ideal Alternating Updates

The alternating bridge-coupling updates can be viewed as block-coordinate descent for the discretized metric-action objective. For each adjacent time interval k, let

$$\Pi_k = \Pi(\hat{\rho}_k, \hat{\rho}_{k+1})$$

denote the feasible set of empirical couplings, and define the finite-dimensional objective

$$\mathcal{J}(\theta, \{\pi_k\}_{k=0}^{K-1}) = \sum_{k=0}^{K-1} \sum_{i,j} \pi_{ij}^{(k)} c_{ij}^{\text{path}}(\theta), \tag{26}$$

where $c_{ij}^{\text{path}}(\theta)$ is the discretized path-action cost in Eq. (9). This objective is the full-batch version of the metric-action term optimized during the bridge update, using the same path-action quadrature as the coupling update.

Proposition F.1 (Monotonicity under exact block updates)**.** *Assume that, at iteration r, the bridge update computes a global minimizer*

$$\theta^{r+1} \in \arg\min_\theta \mathcal{J}(\theta, \{\pi_k^r\}_{k=0}^{K-1}),$$

and the coupling update computes, for each k, a global minimizer

$$\pi_k^{r+1} \in \arg\min_{\pi_k \in \Pi_k} \sum_{i,j} \pi_{ij}^{(k)} c_{ij}^{\text{path}}(\theta^{r+1}).$$

Then the joint metric-action objective is non-increasing:

$$\mathcal{J}(\theta^{r+1}, \{\pi_k^{r+1}\}_{k=0}^{K-1}) \le \mathcal{J}(\theta^r, \{\pi_k^r\}_{k=0}^{K-1}). \tag{27}$$

Moreover, the decrease is strict whenever either the bridge block or at least one coupling block achieves a strict improvement over the previous iterate.

Proof. By the optimality of the bridge update with $\{\pi_k^r\}$ fixed,

$$\mathcal{J}(\theta^{r+1}, \{\pi_k^r\}_{k=0}^{K-1}) \le \mathcal{J}(\theta^r, \{\pi_k^r\}_{k=0}^{K-1}).$$

By the optimality of each coupling update with θ^{r+1} fixed,

$$\sum_{i,j} \pi_{ij}^{(k),r+1} c_{ij}^{\text{path}}(\theta^{r+1}) \le \sum_{i,j} \pi_{ij}^{(k),r} c_{ij}^{\text{path}}(\theta^{r+1}) \quad \text{for every } k.$$

Summing these inequalities over k gives

$$\mathcal{J}(\theta^{r+1}, \{\pi_k^{r+1}\}_{k=0}^{K-1}) \le \mathcal{J}(\theta^{r+1}, \{\pi_k^r\}_{k=0}^{K-1}).$$

Combining the two inequalities proves monotonicity. If either inequality is strict, the combined decrease is strict. □

Because $G_k(x,t) = I + \alpha C_N^{(k)}(x,t)$ is positive definite, every path-action cost is nonnegative; therefore the sequence of ideal objective values is bounded below by zero and hence converges as a sequence of numbers. This does not imply convergence to a global optimum, nor does it imply uniqueness of the bridge or coupling. Equality can occur when a block update returns an equivalent minimizer or when the current block is already optimal.

Relation to the implemented algorithm. The proposition applies to the ideal metric-action problem in Eq. (26). The implemented PACE training approximates this scheme with stochastic minibatches, a neural bridge optimized by finite gradient steps, periodic rather than continuous rematching, and optional stabilizing regularizers. These choices are used for scalability and numerical stability, but they do not provide a per-gradient-step strict decrease guarantee for the realized neural training trajectory. The monotonic result should therefore be read as the optimization principle behind the alternating updates, while the empirical sections evaluate the behavior of the practical stochastic implementation.

G. Stage 1 Regularizers

PACE Stage 1 optimizes a metric action together with an optional regularization term:

$$\mathcal{L}_{\text{bridge}} = \lambda_{\text{metric}} \mathcal{L}_{\text{metric}} + \lambda_{\text{reg}} \mathcal{L}_{\text{reg}}. \tag{28}$$

The metric-action term is the discretized version of Eq. (8). The regularization term can include the implementation-level stabilizers below; in our experiments, this corresponds to a weighted combination

$$\lambda_{\text{reg}} \mathcal{L}_{\text{reg}} = \lambda_{\text{coh}} \mathcal{L}_{\text{coh}} + \lambda_{\text{orth}} \mathcal{L}_{\text{orth}}.$$

Cross-segment velocity coherence. Let (x_a, t_a, v_a) and (x_b, t_b, v_b) denote generated bridge points and velocities from different adjacent segments. PACE constructs Gaussian space-time weights

$$W_{ab} = \exp\left(-\frac{\|x_a - x_b\|^2}{\sigma_{x,a}\sigma_{x,b}}\right) \exp\left(-\frac{|t_a - t_b|^2}{\sigma_{t,a}\sigma_{t,b}}\right) \times \mathbf{1}\{\text{seg}(a) \ne \text{seg}(b)\}, \tag{29}$$

where the bandwidths are estimated from local projector variation. The coherence loss penalizes nearby generated points from different segments when their normalized velocities disagree:

$$\mathcal{L}_{\text{coh}} = \frac{\sum_{a,b} W_{ab}\left(1 - \hat{v}_a^\top \hat{v}_b\right)}{\sum_{a,b} W_{ab} + \varepsilon}, \qquad \hat{v}_a = \frac{v_a}{\|v_a\| + \varepsilon}. \tag{30}$$

Normal-motion suppression. For generated bridge points, PACE estimates a local normal projector and penalizes the normal component of the generated velocity:

$$\mathcal{L}_{\text{orth}} = \frac{1}{|\mathcal{G}|} \sum_{(x,t,v)\in\mathcal{G}} \|P_N(x,t)v\|^2. \tag{31}$$

In 2D this reduces to a squared dot product with the locally estimated normal vector. In higher dimensions it uses the full normal-space projector $P_N = I - P_T$.

H. High-Dimensional Concentration Effects

The high-dimensional experiments in Section 4 operate in a regime where Euclidean probability mass and pairwise costs are strongly concentrated. This section explains the diagnostics used in Figure 4 and why concentration affects OT, MMD, and nearest-neighbor-based trajectory objectives.

Norm concentration. For $X \sim \mathcal{N}(0, I_d)$, the map $f(x) = \|x\|_2$ is 1-Lipschitz. The Gaussian concentration inequality therefore gives

$$\Pr(|\|X\|_2 - \mathbb{E}\|X\|_2| \ge t) \le 2\exp(-t^2/2), \tag{32}$$

and $\mathbb{E}\|X\|_2 \asymp \sqrt{d}$ implies

$$\frac{\text{Std}(\|X\|_2)}{\mathbb{E}\|X\|_2} = O(d^{-1/2}). \tag{33}$$

This is the standard Lipschitz concentration phenomenon (Ledoux, 2001): after whitening or PCA scaling, most points are pushed toward a thin shell rather than spreading across many radial scales.

Direction and nearest-neighbor concentration. For independent isotropic sub-Gaussian vectors $X, Y \in \mathbb{R}^d$, normalized directions satisfy

$$\left\langle \frac{X}{\|X\|_2}, \frac{Y}{\|Y\|_2} \right\rangle = O_p(d^{-1/2}), \tag{34}$$

so random directions become nearly orthogonal as d grows (Vershynin, 2018). A related nearest-neighbor result states that if the relative variance of distances vanishes,

$$\frac{\mathrm{Var}(\|Q - X_1\|_2)}{\mathbb{E}[\|Q - X_1\|_2]^2} \to 0, \tag{35}$$

then

$$\Pr\left(\frac{D_{\max}^{(d)} - D_{\min}^{(d)}}{D_{\min}^{(d)}} \le \epsilon\right) \to 1 \qquad \text{for every } \epsilon > 0, \tag{36}$$

where $D_{\min}^{(d)}$ and $D_{\max}^{(d)}$ are the nearest and farthest distances from the query point (Beyer et al., 1999). Thus, when distance contrast collapses, the nearest neighbor and farthest neighbor become less distinguishable in relative terms.

Effect on OT, MMD, and flow-matching losses. If two approximately isotropic samples $X, Y \in \mathbb{R}^d$ have coordinate-wise fluctuations with comparable scale, then

$$\|X - Y\|_2^2 = \sum_{j=1}^{d} (X_j - Y_j)^2 \tag{37}$$

is a sum of many coordinate-level contributions. Under standard independence or weak-dependence assumptions, a law-of-large-numbers or sub-Gaussian concentration argument implies that $\|X - Y\|_2^2/d$ concentrates around its mean, with relative fluctuations that typically scale as $O(d^{-1/2})$. For transport objectives,

$$W_2^2(\mu, \nu) = \inf_{\pi \in \Pi(\mu,\nu)} \mathbb{E}_{(x,y)\sim\pi} \|x - y\|_2^2, \tag{38}$$

so concentration directly reduces the dynamic range of the cost matrix used by OT and flow-matching couplings. For kernel metrics,

$$\mathrm{MMD}^2(\mu, \nu) = \mathbb{E}\big[k(x, x') + k(y, y') - 2k(x, y)\big], \tag{39}$$

and a distance-based kernel such as $k(x, y) = \exp(-\|x - y\|_2^2/(2\sigma^2))$ also loses contrast when most $\|x - y\|_2^2$ values occupy a narrow interval. Consequently, different predicted distributions can receive similar numerical losses even when their local geometry differs. This is the metric-degeneration issue encountered by high-dimensional distance-based trajectory methods, including metric and OT flow-matching objectives (Kapuśniak et al., 2024).

Reference thresholds in Figure 4. The first diagnostic is

$$\mathrm{CV}_{\mathrm{norm}} = \frac{\mathrm{Std}(\|X\|_2)}{\mathbb{E}\|X\|_2}. \tag{40}$$

The horizontal reference level 0.3 is a practical warning threshold: below it, one standard deviation of radial variation is less than 30% of the mean radius, so most cells lie in a relatively thin shell and pairwise Euclidean costs are dominated by small angular or local fluctuations. This threshold is not a theorem-specific cutoff; it is a scale marker chosen to make the $O(d^{-1/2})$ collapse visible on the empirical PCA representations.

The second diagnostic compares time separation with within-time dispersion. For snapshot centers c_i, c_j, define

$$R_{\mathrm{time}} = \mathrm{median}_{i<j} \frac{\|c_i - c_j\|_2}{\bar{r}_{ij}},$$
$$\bar{r}_{ij} = \frac{1}{2}\Big(\mathbb{E}_{X\sim\mu_i}\|X - c_i\|_2 + \mathbb{E}_{Y\sim\mu_j}\|Y - c_j\|_2\Big). \tag{41}$$

The reference level 1.0 marks the point where the median displacement between time-point centers is comparable to the typical within-time radius. When $R_{\mathrm{time}} \le 1$, the Euclidean shift between snapshots is no larger than the spread of the snapshots themselves, so time labels are difficult to separate using raw pairwise distances alone. Figure 4 summarizes these diagnostics in the main text. The appendix diagnostics in Figures A.6 and A.7 show the corresponding norm-concentration behavior for iPSC-Liu, OP-Cite, and OP-Multi.

Table A.8. iPSC-Liu (Liu et al., 2020) (10D/50D) per-timepoint results across holdouts $t \in \{4, 8, 12, 16\}$.

Dim	Method	MMD ↓				$\mathcal{W}_1$ ↓				$\mathcal{W}_2$ ↓			
		$t=4$	$t=8$	$t=12$	$t=16$	$t=4$	$t=8$	$t=12$	$t=16$	$t=4$	$t=8$	$t=12$	$t=16$
10D	Action Matching	0.6504	0.6959	0.5132	0.3626	3.8458	4.1608	3.1014	4.0123	4.2076	5.9396	3.4279	3.9222
	Aligned CFM	0.6245	0.5936	0.4051	**0.2345**	3.7937	3.4433	2.5372	**1.9877**	4.2084	4.0761	2.9973	**2.2482**
	CURLY	0.5461	0.6054	0.4936	0.5024	3.8694	3.9773	3.1387	3.4660	4.3490	5.5607	3.4974	3.4336
	DMSB	0.9250	0.7057	0.7448	0.7098	10.5837	4.1953	5.5040	4.9522	10.6553	4.5341	5.6287	5.0190
	MFM	0.5864	0.6674	0.5033	0.3521	3.5972	4.0239	3.2515	2.7539	4.0205	5.0654	3.5968	2.6699
	OT-CFM	0.6039	0.6339	0.4951	0.3251	3.6543	4.0040	3.2932	2.5884	4.0624	5.5807	3.6325	2.5030
	PACE(ours)	**0.5244**	**0.5153**	**0.3113**	0.2871	**3.5918**	**3.2507**	**2.3185**	2.5294	**3.7485**	**3.5755**	**2.7868**	2.6406
50D	Action Matching	**0.3517**	0.3506	0.3278	0.2197	7.2261	8.4554	7.9593	6.8096	7.8273	10.3927	8.5704	7.1567
	Aligned CFM	0.3519	**0.2917**	0.2397	0.1663	7.0562	7.5723	7.5947	7.0302	7.6855	8.2791	8.2483	8.0080
	CURLY	0.3824	0.4189	0.2235	0.2327	8.2766	9.7010	7.6085	6.8715	8.8476	11.2946	8.2990	7.1972
	DMSB	0.7593	0.5730	0.4787	0.4441	14.5899	10.4588	9.7531	8.9456	14.7121	10.7933	10.1192	9.3447
	MFM	0.3539	0.3467	0.2679	0.1728	**7.0197**	9.2505	8.5746	6.3246	**7.6665**	10.5394	9.2502	**6.7254**
	OT-CFM	0.3530	0.3458	0.2802	0.1803	7.1278	9.0608	8.7395	6.4288	7.7653	10.4423	9.3687	6.8054
	PACE(ours)	0.3609	0.3004	**0.2193**	**0.1396**	7.0656	**6.8194**	**6.8718**	**6.2581**	7.6896	**7.0798**	**7.5736**	6.7914

High-dimensional benchmark results. Table A.8 reports the per-timepoint reconstruction metrics for iPSC-Liu (Liu et al., 2020) in 10D and 50D PCA representations, evaluated on holdout time points $t \in \{4, 8, 12, 16\}$. Table A.9 gives the corresponding results for the multimodal OP-Cite and OP-Multi datasets (Lance et al., 2022) in 100D. These tables complement the time-averaged summary in Table 3 and the concentration diagnostics in Figure A.6.

I. iPSC-Liu Results

Figure A.7 shows the norm-concentration diagnostics for iPSC-Liu across increasing PCA dimensions, illustrating the $O(d^{-1/2})$ norm-concentration behavior discussed in Appendix H. These panels correspond to the high-dimensional benchmark experiments reported in Table A.8 and summarized in the main text in Table 3.

Table A.9. OP-Cite and OP-Multi (Lance et al., 2022) (100D) results.

Method	OP-CITE (100D)			OP-MULTI (100D)		
	MMD ↓	$\mathcal{W}_1$ ↓	$\mathcal{W}_2$ ↓	MMD ↓	$\mathcal{W}_1$ ↓	$\mathcal{W}_2$ ↓
Action Matching	0.1753	**9.9388**	**10.0448**	**0.1622**	10.7711	10.8160
Aligned CFM	0.1434	10.7009	10.8094	0.1720	10.8330	10.8826
CURLY	0.2529	11.5163	11.6015	0.2786	12.0015	12.0440
MFM	0.1435	10.4301	10.5409	0.1699	10.6274	10.6702
OT-CFM	0.1448	10.4447	10.5491	0.1662	10.6128	10.6564
PACE(ours)	**0.1409**	10.4574	10.5605	0.1693	**10.5824**	**10.6293**

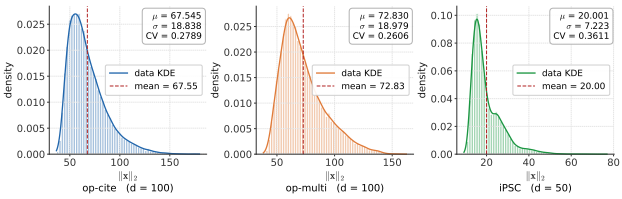

Figure A.6. Norm-concentration diagnostics for iPSC-Liu (Liu et al., 2020) and OP-Cite/OP-Multi (Lance et al., 2022) representations. The panels illustrate the empirical thin-shell behavior summarized by $\mathrm{CV}_{\mathrm{norm}}$, with the 0.3 reference level used as a practical concentration warning threshold.

J. Intuition behind alternating bridge and coupling optimization

Why coupling matters for the bridge. The neural bridge is trained on endpoint pairs sampled from the current coupling. If the coupling is biologically implausible (for example, pairing an early stem cell with a terminally differentiated cell), the bridge must learn a path that traverses the entire developmental manifold in a single segment. Such a path is likely to pass through regions where the metric strongly penalizes normal motion, yielding high action and making it difficult for the network to find a low-action deformation. Conversely, when the coupling pairs cells at nearby pseudotime stages, the displacement is small and largely tangent-aligned, so the bridge can easily learn a geometry-consistent interpolant. In short, the coupling determines the training set for the bridge; wrong pairs give the network an impossible learning problem.

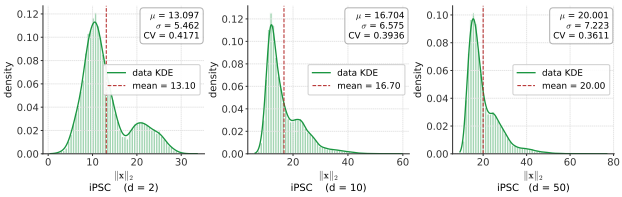

Figure A.7. Norm-concentration diagnostics for iPSC-Liu (Liu et al., 2020) representations. Increasing PCA dimension reduces relative radial variation, consistent with the $O(d^{-1/2})$ norm-concentration behavior described in Appendix H.

Why the bridge matters for the coupling. The coupling update solves an OT problem whose cost matrix is the path action evaluated on the neural bridge (Eq. (9)). If the bridge is untrained, its paths are nearly straight lines and the cost reduces to Euclidean distance; the OT solver then cannot distinguish a biologically plausible pairing from an implausible one. Once the bridge has learned metric-aware paths, the action cost becomes geometry-sensitive. Pairs whose displacement aligns with the local developmental tangent incur low action, while pairs that would require motion across normal (non-developmental) directions incur high action. The bridge therefore transforms an uninformative Euclidean cost into a geometry-aware cost, allowing OT to select biologically meaningful pairings.

Why amortize with a shared neural network. Without amortization, every candidate endpoint pair would require solving an independent boundary-value problem (the geodesic equation) under the state-dependent metric G_k. With $N_k N_{k+1}$ candidate pairs, this is computationally infeasible. The neural bridge amortizes this cost by learning a single parametric family $\gamma_\theta(x, y, \tau)$ that approximates the minimum-action path for all pairs. The approximation need not be perfect at initialization; it only needs to be good enough to provide a more informative cost than Euclidean distance, and it improves as the coupling improves.

K. Adaptive tangent and normal projectors

The weighted local covariance at each anchor point yields eigenvalues $\lambda_1 \le \lambda_2 \le \cdots \le \lambda_d$ and orthonormal eigenvectors $v_1, \ldots, v_d$. The tangent subspace is spanned by the leading (maximum-variance) eigenvectors. Its effective dimension q_r is chosen as the smallest integer such that the cumulative explained variance reaches a prescribed threshold $\tau \in (0, 1)$ (e.g., 0.95):

$$q_r = \min\left\{ q \;:\; \frac{\sum_{j=1}^{q} \lambda_{d-j+1}}{\sum_{j=1}^{d} \lambda_j} \ge \tau \right\}.$$

The tangent projector is $P_T^{(r)} = \sum_{j=1}^{q_r} v_{d-j+1}\, v_{d-j+1}^\top$ and the normal projector is its orthogonal complement $P_N^{(r)} = I - P_T^{(r)}$. In two dimensions this reduces to $P_N^{(r)} = n_r n_r^\top$ with $n_r = v_1$ and $q_r = 1$.

L. Adaptive bandwidth estimation

For each segment k, the spatial and temporal bandwidths $h_x^{(k)}$ and $h_t^{(k)}$ are estimated from the anchor normal bank rather than set by hand. The estimation aggregates information over a small window of anchor snapshots centered on segment k (by default one snapshot on each side). The same local eigendecomposition also yields the tangent subspace

$P_T^{(r)}$ (Appendix K), which is used for bandwidth estimation below but does not enter the metric tensor directly.

Spatial geometry per snapshot. For each anchor snapshot a in the window, PACE computes three quantities from the k nearest neighbors of every cell (excluding the cell itself):

- **Local spatial spacing** $\Delta_x^{(a)}$: the median tangential step size $\|\langle x_j - x_i,\, t_i\rangle\|$ between each cell i and its neighbors j, where t_i is the local tangent direction. This captures how densely cells are spaced along the developmental manifold.
- **Normal spatial rate** $\rho_{N,x}^{(a)}$: the median Frobenius-norm difference $\|P_N^{(j)} - P_N^{(i)}\|_F/\Delta_x^{(a)}$ between the normal projectors of neighboring cells. This measures how rapidly the local geometry changes in space.
- **Tangent spatial rate** $\rho_{T,x}^{(a)}$: the analogous quantity for tangent projectors.

Cross-snapshot temporal rates. For each consecutive pair $(a, a{+}1)$ in the window, PACE matches cells by nearest-neighbor correspondence and computes:

- **Normal temporal rate** $\rho_{N,t}^{(a,a+1)}$: the Frobenius-norm difference $\|P_N^{(\mathrm{nn}(i))} - P_N^{(i)}\|_F/|t_{a+1} - t_a|$ between matched cells, divided by the experimental time gap. This measures how rapidly the local geometry evolves over time.
- **Tangent temporal rate** $\rho_{T,t}^{(a,a+1)}$: the analogous quantity for tangent projectors.

Segment bandwidth assembly. All per-snapshot and cross-snapshot quantities are concatenated and their positive medians are taken, yielding four segment-level scalars: $\Delta_x^{(k)}$, $\rho_{N,x}^{(k)}$, $\rho_{N,t}^{(k)}$, and $\rho_{T,t}^{(k)}$. The metric bandwidths are then

$$h_x^{(k)} = \max\left(\Delta_x^{(k)},\ \frac{1}{\rho_{N,x}^{(k)}}\right), \tag{42}$$

$$c_N^{(k)} = \frac{\rho_{N,t}^{(k)}}{\rho_{N,x}^{(k)}}, \tag{43}$$

$$h_t^{(k)} = \frac{h_x^{(k)}}{c_N^{(k)}}. \tag{44}$$

The spatial bandwidth h_x is the larger of the local spacing and the reciprocal spatial variation scale, preventing the kernel from being narrower than either the point density or the geometry variation. The ratio $c_N^{(k)}$ converts spatial scale into equivalent temporal scale through the speed at which the normal geometry changes in time relative to space. A similar pair $(\sigma_x^{(k)}, \sigma_t^{(k)})$ is computed from the tangent rates for the coupling-refinement kernel, but the metric field uses $(h_x^{(k)}, h_t^{(k)})$.

M. Limitations and Future Work

PACE has several limitations. First, its local metric depends on nearest-neighbor covariance estimates within each snapshot. When data are sparse, noisy, or highly heterogeneous, the estimated tangent and normal subspaces may be unstable; adaptive neighborhood selection may improve robustness.

Second, PACE is optimized with stochastic neural training and periodic rematching. Although Appendix F states a monotonicity property for ideal exact block-coordinate updates, the implemented algorithm is only a scalable approximation and does not guarantee global optimality.

Third, destructive snapshot data do not provide ground-truth correspondences or continuous cell histories. The reported metrics evaluate held-out marginal reconstruction rather than individual trajectory correctness. PACE-inferred paths should be interpreted as plausible geometry-consistent reconstructions, not directly observed cellular histories.

Future work will extend PACE beyond closed-population transport by incorporating birth-death or growth terms (Schiebinger et al., 2019). Another direction is to learn representations that preserve local trajectory geometry in high-dimensional settings, where distance concentration can make coupling costs less discriminative.